Bioelectrochemistry 145 (2022) 108054

Contents lists available at ScienceDirect

Bioelectrochemistry

journal homepage: www.elsevier.com/locate/bioelechem

# Systems-informed genome mining for electroautotrophic microbial production

Anthony J. Abel [a,1], Jacob M. Hilzinger [b,1], Adam P. Arkin [b,c,*], Douglas S. Clark [a,d,*]

[a] Department of Chemical and Biomolecular Engineering, University of California, Berkeley, CA 94720, USA
[b] Department of Bioengineering, University of California, Berkeley, CA 94720, USA
[c] Environmental Genomics and Systems Biology Division, Lawrence Berkeley National Laboratory, 1 Cyclotron Road, Berkeley, CA 94720, USA
[d] Molecular Biophysics and Integrated Bioimaging Division, Lawrence Berkeley National Laboratory, 1 Cyclotron Road, Berkeley, CA 94720, USA

ARTICLE INFO

*Article history:*
Received 21 September 2021
Received in revised form 15 December 2021
Accepted 6 January 2022
Available online 10 January 2022

*Keywords:*
Electromicrobial production
Genome mining
Multiphysics modeling
Microbial electrosynthesis
Extracellular electron transfer

ABSTRACT

Electromicrobial production (EMP) systems can store renewable energy and $CO_2$ in many-carbon molecules inaccessible to abiotic electrochemistry. Here, we develop a multiphysics model to investigate the fundamental and practical limits of EMP enabled by direct electron uptake. We also identify potential electroautotrophic organisms and metabolic engineering strategies to enable electroautotrophy in organisms lacking the native capability. Systematic model comparisons of microbial respiration and carbon fixation strategies revealed that, under aerobic conditions, the $CO_2$ fixation rate is limited to < 6 μmol/cm$^2$/hr by $O_2$ mass transport despite efficient electron utilization. In contrast, anaerobic nitrate respiration enables $CO_2$ fixation rates > 50 μmol/cm$^2$/hr for microbes using the reductive tricarboxylic acid cycle. Phylogenetic analysis, validated by recapitulating experimental demonstrations of electroautotrophy, predicted multiple probable electroautotrophic organisms and a significant number of genetically tractable strains that require heterologous expression of < 5 proteins to gain electroautotrophic function. The model and analysis presented here will guide microbial engineering and reactor design for practical EMP systems.



## 1. Introduction

The capture and conversion of $CO_2$ to fuels, commodity chemicals, and pharmaceutical precursors can help close the anthropogenic carbon cycle. Biological $CO_2$ fixation using plants, algae and cyanobacteria occurs naturally at scale, but biotechnological application of photosynthetic carbon fixation is challenging for several reasons including low conversion rates, low efficiencies, and difficulties with downstream separations [1]. Physicochemical strategies to fix $CO_2$ by generating syngas have also been considered, but extreme operating conditions and low product selectivity for complex hydrocarbons have hindered adaptation [2–4]. Recently, electromicrobial approaches have been proposed in which electrochemical and bioelectrochemical reactions are combined to produce a wide array of chemicals [5,6]. Although naming conventions for such bioelectrochemical systems vary in the literature [6–8], we define electromicrobial production (EMP) processes as any process that converts $CO_2$ into a value-added product, uses electricity as the primary source of energy driving that transformation, and uses microbes to produce the final product. Mediated EMP systems, relying, for example, on electrochemically-derived $H_2$ or $CO_2$-reduction products [9–11], have made substantial progress in recent years. This strategy is particularly promising because it benefits from extensive system modeling and abiotic catalyst discovery efforts [12–15]. However, poor catalyst stability, reliance on rare elements, and potential catalyst toxicity could inhibit the scalability of this method [16–18]. EMP systems based on direct electron transfer (DET) may overcome these issues because they avoid an electrocatalyst by using so-called electroautotrophic microbes that accept electrons from a cathode [6,19]. The inherent regenerative capacity of microbes also makes DET-based EMP (dEMP) an attractive option for chemical production during space exploration missions because carry-along mass and materials resupply challenges are key constraints on long-term or deep-space expeditions [20].

Despite the promise of dEMP systems, product spectrum and production rate bottlenecks have prevented technological realization [21]. Systems developed to date primarily use acetogenic or methanogenic microbes that divert most of their fixed carbon into low-value acetate and methane [22]. Although genetic tools have

* Corresponding authors.
*E-mail addresses:* aparkin@lbl.gov (A.P. Arkin), dsc@berkeley.edu (D.S. Clark).
[1] These authors contributed equally.

https://doi.org/10.1016/j.bioelechem.2022.108054
1567-5394/

recently become available for some of these organisms [23,24], microbial energy conservation strategies severely restrict the achievable product spectrum and selectivity. Microbes supporting electroautotrophy via the Calvin cycle have recently been discovered and are likely to alleviate product spectrum issues [25,26]. However, high throughput platforms for discovery and engineering of novel microbial chassis are in their nascent stages and distinguishing between more and less promising candidates and identifying engineering targets that enable high production rates is challenging [27,28].

Computational models can address this challenge by comparing microbial respiration and carbon fixation strategies. To that end, several models of dEMP systems have been developed, but these have assumed electron uptake interfaces directly with the intracellular $NAD^+$/NADH pool, in contrast to known electron transfer mechanisms [29,30]. Recent energetic calculations to determine the limiting efficiency of EMP systems have addressed this issue, but assumed that aerobic respiration is equally available for all carbon fixation pathways (CFPs) [31]. Moreover, considerations of physiological mechanisms of electron transfer, respiration, and carbon fixation in models that capture relevant physical phenomena remains an outstanding challenge.

Here, we incorporate a physiological, mechanistic understanding of extracellular electron uptake into a comprehensive multiphysics model of dEMP that describes mass transport, electrochemical and acid-base thermodynamics and kinetics, and gas–liquid mass transfer (Fig. 1). In the proposed mechanism, based on the reversible electron conduit in *Shewanella oneidensis* [32], electrons supplied by the cathode are deposited into the quinone pool. A fraction of these electrons is used to produce a proton motive force (PMF) via aerobic or anaerobic nitrate respiration, while the remainder is used along with the PMF to regenerate cellular energy carriers (ATP, NAD(P)H, reduced ferredoxin) consumed in the CFPs. This picture of the electron transfer mechanism is nearly identical to that of Salimijazi *et al.* [31]. We compare the productivity and efficiency of dEMP systems with hypothetical microbes performing carbon fixation with each of four major CFPs and we identify physiological modules that enable the highest productivities. In this model, we use pyruvate as an example product molecule because it is a central metabolite common to the production of many biofuels and biochemicals [33].

We further perform phylogenetic analysis of marker genes for these modules to uncover naturally occurring and/or readily engineerable microbial chassis that require the heterologous expression of only a few proteins. Finally, we identify additional microbial characteristics and reactor concepts that would be extremely beneficial to an industrial dEMP process based on direct electron uptake. Thus, our analysis provides crucial insight into microbial catalyst discovery and engineering and reactor design strategies that can advance dEMP systems from basic science to technological practice.

## 2. Methods

### 2.1. System dimensionality

The model considers a one-dimensional bioelectrochemical reactor for $CO_2$ reduction (Fig. 1a). Three key assumptions were required to reduce the full MES system that is inherently three-dimensional to an appropriate one-dimensional representation. First, the bulk liquid electrolyte/media was assumed to be well-mixed, which avoids concentration gradients that could occur along the direction of electrolyte flow (the vertical axis in Fig. 1a). Second, the model assumes that the geometric area of the reactor (parallel to the plane formed by the vertical axis on the page and the axis extending into and out of the page in Fig. 1a) is much larger than the separation distance between the anode and biocathode layer. This avoids edge effects for ion transport and neglects potentially imperfect current distribution throughout the area of the electrodes. Third, the model assumes that there is no macro-scale variation in the biocathode layer (macro-homogeneity), which allows this layer to be described with a characteristic porosity and conductivity following porous electrode theory [34].

Certain operating or practical conditions could cause any of these assumptions to be faulty in real systems. In such cases, two- or three-dimensional model descriptions would provide further accuracy. For example, insufficient mixing could cause concentration gradients to form in the vertical direction (in Fig. 1a), which would reduce the concentration of $CO_2$ and increase the pH along this axis. In this case, the one-dimensional description could be retained by defining an effectiveness factor related to the Damköhler number, or a complete two-dimensional description of the system could be defined following, for example, similar efforts with abiotic $CO_2$ electrolysis [35]. In either case, insufficient mixing would reduce the productivity of the system, and optimal operation would avoid this issue, so the additional computational expense of the two-dimensional model would provide only marginal benefits for defining the optimal productivity of dEMP systems at this stage of development.

### 2.2. System overview

Species transport for an open electrochemical system must satisfy mass conservation:

$$\frac{\partial c_i}{\partial t} + \frac{\partial N_i}{\partial x} = R_{\mathrm{F},i} + R_{\mathrm{H},i} + R_{\mathrm{CT},i} \tag{1}$$

where $c_i$ is the concentration, $N_i$ is the molar flux, and $R_{\mathrm{F},i}$, $R_{\mathrm{H},i}$, and $R_{\mathrm{CT},i}$ are the net volumetric rates of formation or consumption for species $i$ ($CO_2$, $HCO_3^-$, $CO_3^{2-}$, $H^+$, $OH^-$, $Na^+$, $NO_3^-$) due to gas and electrolyte (F) feed terms, homogeneous (H) chemical reactions, and electrochemical charge transfer (CT) reactions, respectively. $R_{\mathrm{F},i}$ applies only in the well-mixed electrolyte phases where gas and electrolyte feeds are introduced and $R_{\mathrm{CT},i}$ applies only in the porous biocathode layer. The biocathode layer is assumed to be comprised of a porous electrode support structure on which cells grow in a monolayer (Fig. 1b), and therefore could be described as an "artificial" biofilm thickness.

In the following sections, we formulate the equations that govern transport and reactions within the dEMP system, describe assumptions, and report the key parameter values used in our model.

### 2.3. Species transport in the electrolyte boundary layers, membrane, and porous biocathode

The molar flux of species (assuming no net fluid velocity) in dilute electrolyte solutions is written as the sum of diffusive and migrative fluxes:

$$N_i = -D_i \frac{\partial c_i}{\partial x} - z_i u_i F c_i \frac{\partial \phi_l}{\partial x} \tag{2}$$

where $D_i$ and $u_i$ are the diffusivity and mobility (related by the Nernst-Einstein relationship, $u_i = D_i/RT$ for dilute solutions) of species $i$, $z_i$ is the charge number, $F$ is Faraday's constant, and $\phi_l$ is the local electrolyte potential. In the anion exchange membrane (AEM), we reduce diffusion coefficients of anions and cations by a factor of 10 and 100 respectively relative to those in the electrolyte to model a generic anion exchange membrane and assume a fixed background positive unit charge with a 0.5 M concentration, following

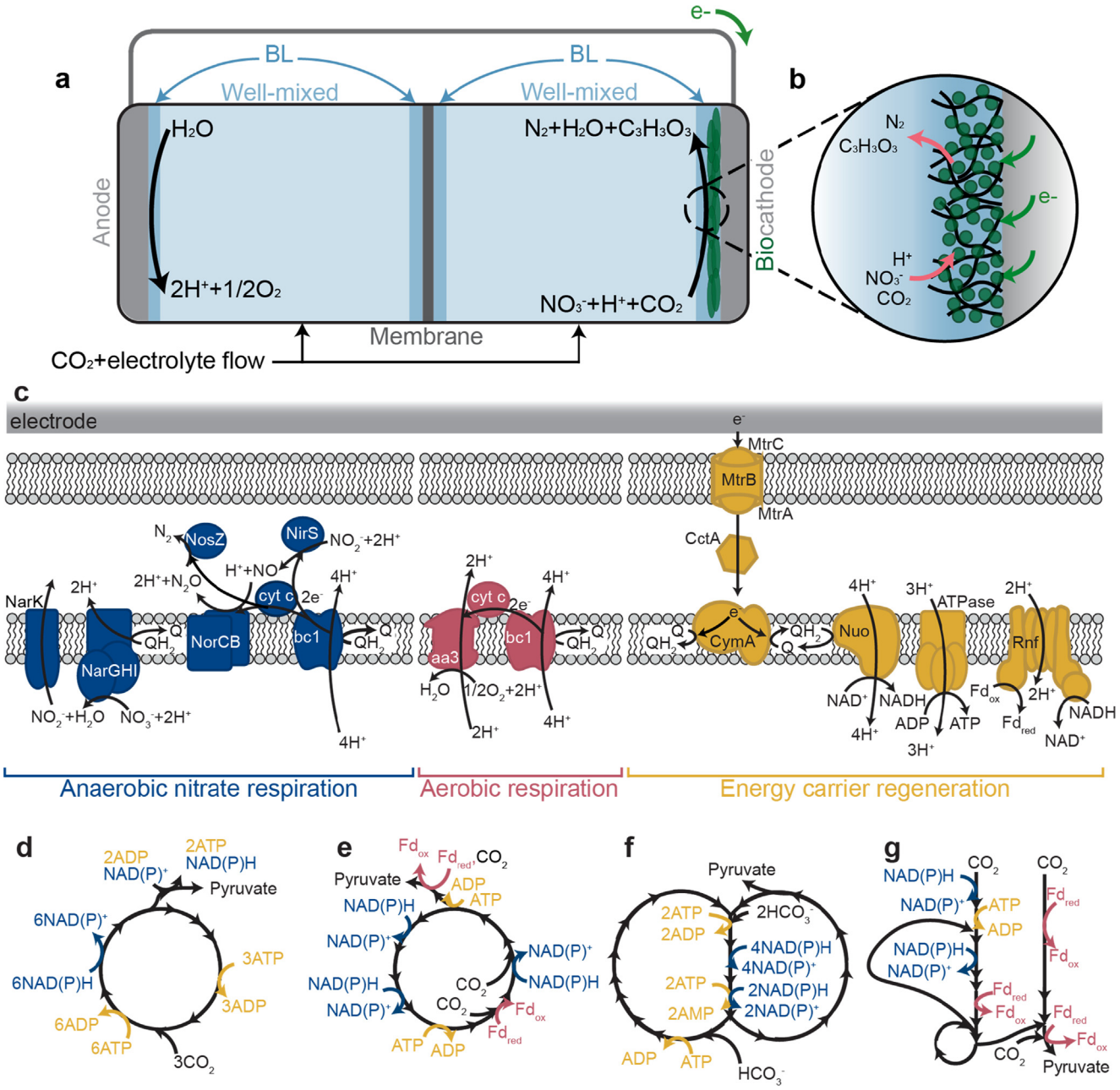


**Fig. 1. Schematic of a one-dimensional EMP reactor and direct electron transfer mechanisms for (an)aerobic carbon fixation.** (**a**) Reactor scheme. Carbon dioxide ($CO_2$) and electrolyte media are fed into well-mixed regions separated by a membrane. (**b**) Direct electron transfer to a microbial biofilm supports carbon fixation to pyruvate using $NO_3^-$ as the terminal electron acceptor. (**c**) Respiratory and energy carrier regeneration mechanisms using $NO_3^-$ and $O_2$ as terminal electron acceptors. (**d**) The Calvin-Benson-Bassham (CBB), (**e**) reductive tricarboxylic acid (rTCA), (**f**) 3-hydroxypropionate bi-cycle (3HP), and (**g**) Wood-Ljungdahl (WL) pathway for carbon fixation to pyruvate shown with reducing equivalent consumption.

Singh *et al.*[36] We also use effective diffusion coefficients within the biocathode layer calculated using the Bruggeman relationship,

$$D_{i,\mathrm{eff}} = \epsilon_p^{3/2} D_i \tag{3}$$

where $\epsilon_p$ is the biofilm porosity. The net ionic current density in the electrolyte ($i_l$) can be calculated from the total ionic flux:

$$i_l = F \sum_i z_i N_i \tag{4}$$

where $F$ is Faraday's constant and $z_i$ is the charge number, following electroneutrality:

$$\sum_i z_i c_i = 0 \tag{5}$$

### 2.4. Gas feed and electrolyte flow in the well-mixed electrolyte

The well-mixed electrolyte regions are assumed to have sufficient convective mixing such that no concentration gradients are formed. Species transport into and out of the boundary layers is considered at the interface between the well-mixed and boundary layer electrolyte phases (Fig. 1a, b). Constant gas feed and electrolyte flow terms in the well-mixed regions are included to describe a continuously operating system, given by

$$R_{\mathrm{F},CO_2} = k_L a\left(K_0 P_{CO_2} - c_{CO_2}\right) \tag{6}$$

$$R_{\mathrm{F},i\neq CO_2} = D\left(c_{i,0} - c_i\right) \tag{7}$$

where $k_L a$ is the volumetric mass-transfer coefficient (in units $s^{-1}$) on the liquid side of the gas/liquid interface, $K_0$ is Henry's constant for $CO_2$ in water, $P_{CO_2}$ is the pressure of $CO_2$ in the gas phase, $D$ is the dilution rate (defined as the inverse space time, or volumetric flow rate divided by reactor volume), and $c_{i,0}$ is the initial or feed concentration of the $i$ th species. The equilibrium of $CO_2$ between the gas and liquid phases, $CO_{2(g)} \leftrightarrow CO_{2(aq)}$, is described by Henry's constant such that

$$K_0 = \frac{c_{CO_2}}{P_{CO_2}} \tag{8}$$

Henry's constant for $CO_2$ depends on the temperature and salinity of the aqueous phase and follows an empirical relationship [37],

$$\ln(K_0) = 93.4517\left(\frac{100}{T}\right) - 60.2409 + 23.3585\ln\left(\frac{T}{100}\right) + S\left(0.023517 - 0.023656\left(\frac{T}{100}\right) + 0.0047036\left(\frac{T}{100}\right)^2\right) \tag{9}$$

where $S$ is the salinity in units g/kg and $T$ is the temperature.

### 2.5. Homogeneous chemical reactions

The acid-base bicarbonate/carbonate and water-dissociation reactions shown below occur in all phases and are treated as kinetic expressions without assuming equilibrium (eq. (15)):

$$CO_{2(aq)} + H_2O \overset{k_{+1},k_{-1}}{\leftrightarrow} H^+ + HCO_3^- \qquad K_1 \tag{10}$$

$$HCO_3^- \overset{k_{+2},k_{-2}}{\leftrightarrow} H^+ + CO_3^{2-} \qquad K_2 \tag{11}$$

$$CO_{2(aq)} + OH^- \overset{k_{+3},k_{-3}}{\leftrightarrow} HCO_3^- \qquad K_3 = K_1/K_w \tag{12}$$

$$HCO_3^- + OH^- \overset{k_{+4},k_{-4}}{\leftrightarrow} CO_3^{2-} + H_2O \qquad K_4 = K_2/K_w \tag{13}$$

$$H_2O \overset{k_w,k_{-w}}{\leftrightarrow} H^+ + OH^- \qquad K_W \tag{14}$$

where $k_{+n}$ and $k_{-n}$ are the forward and reverse rate constants, respectively, and $K_n$ is the equilibrium constant for the $n$ th reaction. Source and sink terms resulting from these reactions are compiled in $R_{H,i}$, written as

$$R_{H,i} = \sum_n \nu_i \left(k_{+n}\prod_{\nu_i<0} c_i - k_{-n}\prod_{\nu_i>0} c_i\right) \tag{15}$$

where $\nu_i$ is the stoichiometric coefficient of species $i$ for the $n$ th reaction and reverse rate constants are calculated from

$$k_{-n} = \frac{k_{+n}}{K_n} \tag{16}$$

### 2.6. Electrode reactions – anode

The surface reaction at the anode is the oxidation of water:

$$H_2O \rightarrow \frac{1}{2}O_2 + 2H^+ + 2e^- \qquad E^0_{OER} \tag{17}$$

where $E^0_{OER}$ is the equilibrium potential of the oxygen evolution half-cell reaction (OER) at standard state. The anode reaction is related to species transport by a flux boundary condition at the electrode surface,

$$N_i = \frac{-\nu_i i_R}{nF} \tag{18}$$

where $i_R$ is the reaction current density and $n$ is the number of electrons participating in the electrode reaction. We model charge transfer kinetics at the anode using Butler-Volmer kinetics:

$$i_R = i_0\left[\left(\frac{c_{red}}{c_{red,0}}\right)^{\gamma_{red}}\exp\left(\frac{\alpha_a F\eta}{RT}\right) - \left(\frac{c_{ox}}{c_{ox,0}}\right)^{\gamma_{ox}}\exp\left(\frac{\alpha_c F\eta}{RT}\right)\right] \tag{19}$$

where $i_0$ is the constant exchange current density, $\gamma_{red/ox}$ is the reaction order with respect to a reactant, $\alpha_{a/c}$ is the anodic/cathodic transfer coefficient, and $\eta$ is the overpotential. Kinetic parameters for the OER are sourced from Haussener *et al.*[38]. The overpotential is defined according to

$$\eta = \phi_s - \phi_l - E \tag{20}$$

where $\phi_s$ is the electrode potential, $\phi_l$ is the electrolyte potential, and $E$ is the half-cell equilibrium potential.

Because water oxidation creates acidic conditions near the anode surface, bicarbonate and carbonate species will be converted to aqueous $CO_2$ according to Le Chatelier's principle. To avoid the unrealistic supersaturation of $CO_2$ in the electrolyte this would cause, we describe evolution of $CO_2$ in the electrolyte as

$$R_{CO_2,evolution} = -\gamma\left(\frac{c_{CO_2}}{K_0 f_{CO_2}}\right)^2 \qquad \frac{c_{CO_2}}{K_0 P_{CO_2}} > 1$$
$$= 0 \qquad \frac{c_{CO_2}}{K_0 P_{CO_2}} \le 1$$

where $\gamma$ is the releasing coefficient and $c_{CO_2}/K_0 P_{CO_2}$ is the supersaturation ratio. This formulation was originally reported by Wilt, and was utilized to describe $CO_2$ evolution in abiotic electrochemical systems previously[15,36,39,40].

### 2.7. Electrode reactions – biocathode

Electrons supplied from the solid electrode support Fig. 1b) must be energetic enough to reduce heme groups in the exterior electron conduit protein, MtrC (corresponding to a redox potential below ~−100 mV *vs.* SHE, see supplementary note 8). These electrons are passed through the MtrCAB conduit and ultimately to CymA or similar inner membrane proteins, where they are used to reduce the quinone pool at a redox potential between −80 and +100 mV *vs.* SHE (Fig. 1c) [32,41]. Electrons in the quinone pool are not energetic enough to drive $NAD^+$ reduction by themselves, so reverse electron flow is required for (re-)generation of energy carriers (reducing equivalents) such as NADH, ATP, and ferredoxins [42]. In our proposed scheme, which is experimentally supported by the analysis of Rowe *et al.*[32] and analogous to a similar process in *Acidithiobacillus ferrooxidans*[25], a portion of the electrons deposited into the quinone pool travel energetically downhill to reduce a terminal electron acceptor (*e.g.*, $NO_3^-$, +740 mV *vs.* SHE). The released energy from this process is conserved by a proton motive force, which is used to drive the thermodynamically uphill energy carrier (re-)generation reactions (Fig. 1c). Once these energy carriers are generated, carbon fixation processes function as normal. By tracking the electrons through each step of this process, we derive the overall electron demand per fixed $CO_2$ molecule and use this as the overall (bio)electrochemical reaction occurring throughout the biocathode layer ($R_{CT}$).

We begin with the physiology of direct electron transfer through the MtrCAB electron conduit (Fig. 1c) to determine the stoichiometry of $CO_2$ reduction to pyruvate for four major carbon fixation pathways (Fig. 1d–g) using either aerobic or anaerobic nitrate respiration. All processes start with quinone (Q) reduction,

$$Q + 2H^+_{in} + 2e^- \rightarrow QH_2 \tag{22}$$

using the MtrCAB/CctA/CymA electron conduit native to *S. oneidensis* [32,42–44]. Thermodynamically downhill electron transfer processes (respiration) are used to generate a proton motive force necessary to drive regeneration of energy carriers (*e.g.*, NADH). For aerobic respiration, the respiratory complex III (*e.g.* the *bc1* complex) oxidizes a quinol, pumping protons across the inner membrane [45,46]:

$$QH_2 + 2H^+{}_{in} \rightarrow Q + 4H^+{}_{out} + 2e^- \tag{23}$$

where the subscripts "in" and "out" refer to ion locations in the intracellular space and periplasm, respectively. The two electrons liberated in this process are transported by *c*-type cytochromes to respiratory complex IV (*e.g.* the *aa3* complex), which transports two additional protons across the inner membrane and reduces $O_2$ to $H_2O$ [45,47]:

$$\frac{1}{2}O_2 + 2H^+ + 2e^- + 2H^+{}_{in} \rightarrow H_2O + 2H^+{}_{out} \tag{24}$$

For anaerobic nitrate respiration, quinols are consumed both to pump protons via respiratory complex III, eq. (23), and to reduce $NO_3^-$ to nitrite ($NO_2^-$) using, *e.g.* the Nar complex [48]:

$$NO_3{}^- + 2H^+ + QH_2 \rightarrow NO_2{}^- + H_2O + Q + 2H^+{}_{out} \tag{25}$$

Further reactions consume electrons liberated by quinol oxidation to complete the reduction of $NO_2^-$ to $N_2$ [48]:

$$NO_2{}^- + 2H^+ + e^- \rightarrow NO + H_2O \tag{26}$$

$$NO + H^+ + e^- \rightarrow \frac{1}{2}N_2O + \frac{1}{2}H_2O \tag{27}$$

$$N_2O + 2H^+ + 2e^- \rightarrow N_2 + H_2O \tag{28}$$

Carbon fixation pathways require NAD(P)H, ATP, and/or reduced ferredoxins ($Fd_{red}$) as reducing equivalents [49]. Cells can regenerate these reducing equivalents by translocating protons (PMF consumption) using, *e.g.*, the Nuo complex for NADH [50], ATP synthase for ATP [51], and the Rnf complex for ferredoxins [52–54] according to

$$NAD^+ + 4H^+{}_{out} + QH_2 \rightarrow NADH + 4H^+{}_{in} + Q \tag{29}$$

$$ADP + 3H^+{}_{out} \rightarrow ATP + 3H^+{}_{in} \tag{30}$$

$$Fd_{ox} + NADH + 2H^+{}_{out} \rightarrow Fd_{red} + NAD^+ + 2H^+{}_{in} \tag{31}$$

We use these regeneration mechanisms to determine the stoichiometry (number of reduced molecules produced per number of electrons consumed) for aerobic or anaerobic nitrate respiration (Table S1). Because carbon fixation pathways have different energy carrier requirements, we also derive the overall stoichiometry for $CO_2$ reduction to pyruvic acid (pyruvate) (Table S2). For the aerotolerant carbon fixation pathways (Calvin cycle, eq. (32), Fuchs-Holo bi-cycle, eq. (33)), the cathodic half-cell reactions using aerobic respiration are

$$3CO_2 + 3\frac{5}{12}O_2 + 23\frac{2}{3}H^+ + 23\frac{2}{3}e^- \rightarrow C_3H_4O_3 + 9\frac{5}{6}H_2O \tag{32}$$

$$3CO_2 + 3\frac{3}{4}O_2 + 25H^+ + 25e^- \rightarrow C_3H_4O_3 + 10\frac{1}{2}H_2O \tag{33}$$

For carbon fixation pathways using $NO_3^-$ as the terminal electron acceptor, the half-cell reactions are

$$3CO_2 + 10\frac{1}{4}NO_3{}^- + 71\frac{1}{2}H^+ + 61\frac{1}{4}e^- \rightarrow C_3H_4O_3 + 5\frac{1}{8}N_2 + 33\frac{3}{4}H_2O \tag{34}$$

$$3CO_2 + 7\frac{1}{2}NO_3{}^- + 55H^+ + 47\frac{1}{2}e^- \rightarrow C_3H_4O_3 + 3\frac{1}{4}N_2 + 25\frac{1}{2}H_2O \tag{35}$$

$$3CO_2 + 11\frac{1}{4}NO_3{}^- + 77\frac{1}{2}H^+ + 66\frac{1}{4}e^- \rightarrow C_3H_4O_3 + 5\frac{5}{8}N_2 + 36\frac{3}{4}H_2O \tag{36}$$

$$3CO_2 + 7\frac{1}{4}NO_3{}^- + 53\frac{1}{2}H^+ + 46\frac{1}{4}e^- \rightarrow C_3H_4O_3 + 3\frac{1}{8}N_2 + 24\frac{3}{4}H_2O \tag{37}$$

where eq. (34) is for the Calvin cycle, eq. (35) is for the rTCA cycle, eq. (36) is for the Fuchs-Holo bicycle (F-H), and eq. (37) is for the Wood-Ljungdahl (WL) pathway.

Biocathode reactions, eq. (32)-(37), relate $CO_2$-fixing reactions to species transport in the biocathode layer by

$$R_{CT,i} = \frac{\nu_i a_v i_B}{nF} \tag{38}$$

where $a_v$ is the active specific surface area of the biocathode and $i_B$ is the current density on the biocathode surfaces. The active specific surface area is calculated based on the geometric assumptions described above, resulting in

$$a_v = \frac{3(1-\epsilon_p)}{r_{cell}} \tag{39}$$

where $r_{cell}$ is the radius of the spherical microbe.

The current density, and therefore the $CO_2$-fixation rate, can be limited by any of three factors comprising several processes. First, the $CO_2$-fixation rate could be limited by the enzyme kinetics of carbon fixation. Second, this rate could be limited by the kinetics of electron transfer, including electron uptake by cells, passage through the electron conduit (MtrCAB), or regeneration of reducing equivalents (*e.g.*, NADH). Third, it could be limited by the availability of a necessary substrate (*e.g.*, $CO_2$). Of these processes, our analysis indicates three could limit the $CO_2$ fixation rate: the enzyme kinetics of carbon fixation, the electron uptake charge transfer reaction, and the availability of $CO_2$ (see Supplementary Note 10 for a detailed description).

To account for the rate limit set by the enzyme kinetics, which depends on the turnover number of the rate-limiting enzyme in the carbon fixation pathway, we impose a limit on $i_B$ via

$$i_B = \frac{i_R}{1 + \left|\frac{i_R}{i_{lim}}\right|} \tag{40}$$

where $i_{lim}$ is the biomass-limited current density. We calculate the biomass-limited current density by projecting the enzymatic rate limit to the total cell surface:

$$i_{lim} = nFk_{cat}\left(\frac{n_E}{N_{Av}V_{cell}}\right)\left(\frac{1-\epsilon_p}{a_v}\right) \tag{41}$$

where $k_{cat}$ is the enzyme turnover number (units $s^{-1}$), $n_E$ is the enzyme amount in each cell (units $cell^{-1}$) $N_{Av}$ is Avogadro's number, and $V_{cell}$ is the microbe volume. This formulation for the limiting current density relies on the fact that the rate of intracellular diffusion of substrates is much faster than the rate-limiting reaction step in carbon fixation pathways (see Supplementary Note 1 for calculations that validate this description), indicating that energy carriers and $CO_2$ have complete and effectively immediate access to intracellular enzymes once generated at or delivered to the cell surface.

The charge transfer reaction current density limit, $i_R$ in Eq. (40), is defined using Butler-Volmer kinetics, Eq. (19), which describes the rate limit set by electron transfer from the solid electrode support to the electron conduit proteins. The Butler-Volmer equation also accounts for the availability of $CO_2$ based on the pre-exponential factor $\left(\frac{c_{ox}}{c_{ox,0}}\right)^{\gamma_{ox}}$.

### 2.8. Electron transport in the solid electrode

Electron transport in the solid electrode regions is governed by charge conservation and Ohm's law, given by

$$\nabla i_s = -\nabla i_l = -a_v i_B \tag{42}$$

$$i_s = \kappa_s \frac{\partial \phi_s}{\partial x} \tag{43}$$

where $i_s$ is the electrode current density and $\kappa_s$ is the anode/biocathode conductivity. The conductivity in the biocathode is modified by a Bruggeman correction:

$$\kappa_{s,eff} = (1-\epsilon_p)^{1.5}\kappa_s \tag{44}$$

### 2.9. Numerical method

The governing equations are solved using the MUMPS general solver in COMSOL Multiphysics 5.4. The modeling domain has a maximum element size of 10 μm in the well-mixed regions and 0.5 μm near boundaries to capture steep concentration gradients; the solution was independent of increasing mesh resolution. Model parameters are listed in Table S3. The potential in the reactor is calculated relative to zero potential at the cathode base and potential or current density is applied as a boundary condition at the anode.

### 2.10. Reactor model analysis

The total system voltage ($V_{system}$) is calculated according to [55].

$$V_{system} = \Delta E^0 + V^{Ohmic} + U^{Nernst} + \eta_A + \eta_{BC} \tag{45}$$

where $\Delta E^0$ is the standard state potential difference between the anode and biocathode reactions ($\Delta E^0 = E^0_{OER} - E^0_{CO_2RR}$), $V^{Ohmic}$ is the total ohmic overpotential due to liquid and solid phase resistivity, $U^{Nernst}$ is the Nernst potential that accounts for deviations away from standard state concentrations of reacting species, and $\eta_A$ and $\eta_{BC}$ are the kinetic (activation) overpotentials associated with the anode ($A$) and biocathode layer ($BC$) charge transfer reactions as defined in Eq. (20).

### 2.11. Construction and analysis of phylogenetic trees

Seed sequences for marker genes [56–58] of each pathway (Table S4) were fed to JackHMMER for homology searches [59]. Protein identifiers from the JackHMMER output were used to retrieve full-length protein sequences from Uniprot (The Uniprot Consortium 2019). Protein alignments were created using MAFTT [60,61]. Maximum likelihood trees for each protein search result were built using FastTree 2 [62]. Trees were visualized with Iroki [63]. Trees were manually annotated through a combination of conserved protein domain information (The Uniprot Consortium 2019), inclusion of characterized proteins when available [64,65], and nearest characterized protein information for uncharacterized proteins [65]. Protein sequences corresponding to each marker gene were extracted from the phylogenies using the R package ape [66]. Extracted protein sequences for all marker genes were used to construct a table containing gene presence or absence information for each genome in the dataset (Table S6). Phylogenetic trees displaying gene presence and absence data were built using 16S sequences that were aligned using MAFFT [60,61], built using FastTree 2 [62], and visualized using the Interactive Tree of Life [67] and annotated using taxonomy data from NCBI. Presence of genetic tools was established through a literature search (Table S5).

MtrC from *Shewanella oneidensis* was used as the seed sequence in generating the multi-heme cytochrome phylogeny (Table S4). The JackHMMER output was filtered to exclude sequences with less than eight heme motifs (CxxCH or CxxxCH), and those sequences outside the range of sequence lengths of sequences containing exactly ten heme motifs (188–1434 amino acids). Biochemically characterized multi-heme cytochromes were used to annotate the phylogeny: MtrC [68], OmcA [69], MtrF [69], PioA [26,70], MtoA [71], DmsE [72], MtrA [69], MtrD [69], and ExtA [73]. Although MtrA/D are components of three-subunit electron conduits with MtrC/F, members of this clade, such as PioA and MtoA, are components of two-subunit electron conduits. While DmsE is characterized as being a DMSO reductase, this protein clustered very closely to MtrA and MtrD, and we were therefore unable to separate putative DMSO reductases from cytochromes that may interact with an electrode. Thus, all members of the DmsE/MtrA/PioA/MtoA-family clade of proteins were kept for downstream analysis as potential multi-heme cytochromes involved in direct electron transfer with an electrode.

## 3. Results

### 3.1. System overview

The model (see Methods for additional detail) considers a one-dimensional bioelectrochemical reactor for $CO_2$ reduction (Fig. 1a). The reactor has well-mixed anolyte and catholyte regions that are replenished at a fixed dilution rate and to which $CO_2$ is constantly supplied at a fixed partial pressure. These regions are separated by an anion exchange membrane (AEM) and fluid boundary layers, which also separate the well-mixed phases from the anode surface and the biocathode layer. The chemical species in each chamber are dissolved $CO_2$, dissolved $O_2$ (in the case of aerobic operation), bicarbonate anions ($HCO_3^-$), carbonate anions ($CO_3^{2-}$), protons ($H^+$), hydroxide anions ($OH^-$), sodium cations ($Na^+$), and nitrate anions ($NO_3^-$). The biocathode is assumed to be comprised of a porous electrode support with a characteristic porosity and electrical (Ohmic) conductivity, supporting an active biomass density of 1 cell per $\mu m^3$ (roughly equivalent to a biomass density of 0.4 gCDW/$cm^3$, Fig. 1b).

We use the physiology of direct electron transfer through the MtrCAB electron conduit (Fig. 1c) to determine the stoichiometry of $CO_2$ reduction to pyruvate for four major CFPs (Fig. 1d-g) using either aerobic or anaerobic nitrate respiration (see Methods for additional detail). Although this particular physiology is not found in any known organisms, several factors justify this choice as a representative system for modeling. First, the MtrCAB electron conduit has been shown to be reversible, resulting in electron uptake and deposition into the quinone pool [32,41]. Second, known electron conduit proteins interact primarily with the quinone pool and not with other cellular energy carriers (*e.g.*, NADH).[74] Third, the quinone pool is less energetic than other energy carriers (redox potential of ~ -80 mV *vs*. SHE as compared to ~ -320 mV *vs*. SHE for the $NAD^+$/NADH redox couple), so this assumption is more likely to underestimate the efficiency of cellular energy acquisition *via* electron uptake than to overestimate it. We also assume that the high pH (resulting from the microbial consumption of protons associated with respiration and carbon fix-

ation) will have no effect on cellular activity, which allows us to calculate productivity limits imposed by enzymatic activity or chemical species transport. We note that this is realizable only by alkaliphiles or organisms that have been adapted to alkaline environments. We consider this, and other, microbial engineering targets in the discussion below.

### 3.2. Comparing microbial respiration and carbon fixation pathways

The terminal electron acceptor and CFP constrain the efficiency and productivity of dEMP systems. Because $O_2$ is more electronegative than $NO_3^-$, aerobic respiration allows microbes to divert a higher fraction of electrons to energy carrier regeneration and therefore carbon fixation (Tables S1 and S2). For microbes using the Calvin-Benson-Bassham (CBB) cycle, aerobic respiration uses only 23.67 electrons per pyruvate molecule, while anaerobic nitrate respiration requires 61.25 electrons for the equivalent reaction. Under anaerobic conditions, obligately anaerobic CFPs use electrons more efficiently than aero-tolerant pathways: the reductive tricarboxylic acid (rTCA) cycle and the Wood-Ljungdahl pathway (WLP) require 47.5 and 46.25 electrons per pyruvate, respectively, while the CBB cycle and the 3-hydroxypropionate (3-HP) bi-cycle need 61.25 and 66.25 electrons. The rate-limiting step in carbon-fixing reactions must also be considered when evaluating productivity. While the WLP uses electrons most efficiently, the enzymatic processes are rate-limited compared to other CFPs (Table S3, Supplementary note 2), so more biomass would be needed to fix carbon at equal rates.

To determine the impacts these competing constraints have on dEMP systems, we calculated the pyruvate production rate as a function of $O_2$ partial pressure for microbes using the CBB cycle to fix carbon with $O_2$ as the terminal electron acceptor (Fig. 2a) and pyruvate production versus applied voltage for microbes using $NO_3^-$ as the terminal electron acceptor and different CFPs (Fig. 2b). For aerobic respiration, pyruvate production remains < 2 μmol/cm$^2$/hr even at $O_2$ partial pressures 5-fold greater than in the atmosphere ($P_{O_2}$ = 1 atm) due mainly to the low solubility and corresponding transport limitations of $O_2$ in aqueous solutions (Supplementary note 3). In contrast, pyruvate production using anaerobic nitrate respiration reaches ~ 16.9 μmol/cm$^2$/hr at ~ 2.3 V for microbes using the rTCA cycle before the system becomes $CO_2$ transport limited, defined as the point at which the $CO_2$ concentration reaches ~ 0 mM at the base of the biofilm (current collector). It is worth noting that the applied voltage reported in Fig. 2b corresponds to the total system voltage, including the thermodynamic voltage, kinetic overpotentials associated with both the water oxidation reaction (at the anode) and the $CO_2$-fixation reaction (throughout the biocathode), the Nernst overpotential, and solid and liquid Ohmic overpotentials. Maximum pyruvate production rates for microbes using the CBB cycle (~7.0 μmol/cm$^2$/hr), 3-HP cycle (~4.4 μmol/cm$^2$/hr), and WLP (~1.9 μmol/cm$^2$/hr) are limited by the biomass available to fix carbon in 50 μm biofilms well before $CO_2$ transport becomes rate limiting.

### 3.3. Biofilm thickness effects on productivity

Because electroautotrophic biofilms are typically only a few monolayers thick, 3D electrodes of varying geometries have been used to increase the effective biofilm thickness by orders of magnitude [75,76]. For example, Jourdin *et al.* was able to grow a ~5–10 μm-thick biofilm throughout a 3D electrode with an active surface area of ~2600 m$^{-1}$ and a total thickness of ~1 cm [77]. To simplify the modeling domain, we treat this complex structure as a porous electrode with a characteristic porosity, conductivity, and biomass density, following similar approaches to modeling gas diffusion electrodes [13]. Because the carbon fixation reaction can be treated as occurring on the cell surface (Supplementary note 1), this approach does not result in any loss in model validity or generality. This effective biofilm thickness plays an important and complex role in determining both the total carbon fixation rate and the energy efficiency of the system. Increasing the biofilm thickness increases the biomass available to fix carbon, enabling a higher total electron uptake rate by increasing the biomass-limited production rate. However, $CO_2$ (and/or $NO_3^-$) transport through the biofilm will eventually impose an upper bound on the reaction rate. We plot the voltage necessary to achieve selected pyruvate production rates as a function of biofilm thickness for microbes using the rTCA cycle (Fig. 3a) or CBB cycle (Fig. 3b). For microbes using the CBB cycle, ~3.5-fold thicker biofilms are needed to achieve equivalent production rates because of the lower turnover number for the rate-limiting enzyme, RuBisCo, and the ~ 29% less efficient use of electrons. These factors also limit the achievable productivity of microbes using the CBB cycle to < 12 μmol/cm$^2$/hr because thicker biofilms present a longer distance for $CO_2$ diffusion.

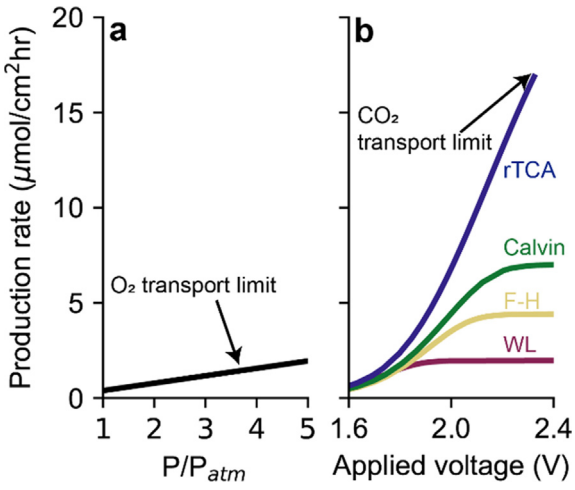


**Fig. 2. Effects of terminal electron acceptor and carbon fixation pathway on reactor operation.** Pyruvate production rate at equivalent biofilm thickness (50 μm) as a function of (**a**) $O_2$ pressure supplied to the reactor headspace relative to atmospheric $O_2$ for microbes using the Calvin cycle with $O_2$ as the terminal electron acceptor, and (**b**) applied voltage for each carbon fixation pathway with $NO_3^-$ as the terminal electron acceptor. Reactor conditions: initial pH = 7.4, 0.25 M $NaNO_3$, D = 5 hr$^{-1}$.

For both CFPs, increasing the biofilm thickness has a non-linear effect on the applied voltage necessary to achieve a fixed production rate (Fig. 3a, b). The initial rapid decline, and the following plateau over a wide thickness range, is due to the competing impacts of the activation overpotential for the $CO_2$ reduction reaction ($CO_2$-RR) and transport-associated (Nernst and Ohmic) overpotentials (Supplementary note 4). To describe these trends, we show the applied voltage breakdown for microbes using the rTCA (Fig. 3c, d) or CBB (Fig. 3e, f) cycles at representative biofilm thicknesses. For microbes using the rTCA cycle, increasing the effective biofilm thickness from 35 μm (Fig. 3c) to 50 μm (Fig. 3d) increases the maximum current density the biofilm can support from ~ 21.5 mA/cm$^2$ to ~ 31 mA/cm$^2$, but $CO_2$ transport restricts the current density to 21.5 mA/cm$^2$ for the 50-μm biofilm. Increasing the effective biofilm thickness reduces the applied voltage necessary to achieve a given production rate (Fig. 3a). The difference is slight at lower rates because increased Ohmic loss (due to electron conduction through a thicker biofilm) mostly balances the reduced activation overpotential associated with the $CO_2$RR (Fig. 3c, d). However, as the production rate approaches the biomass-limited rate for the

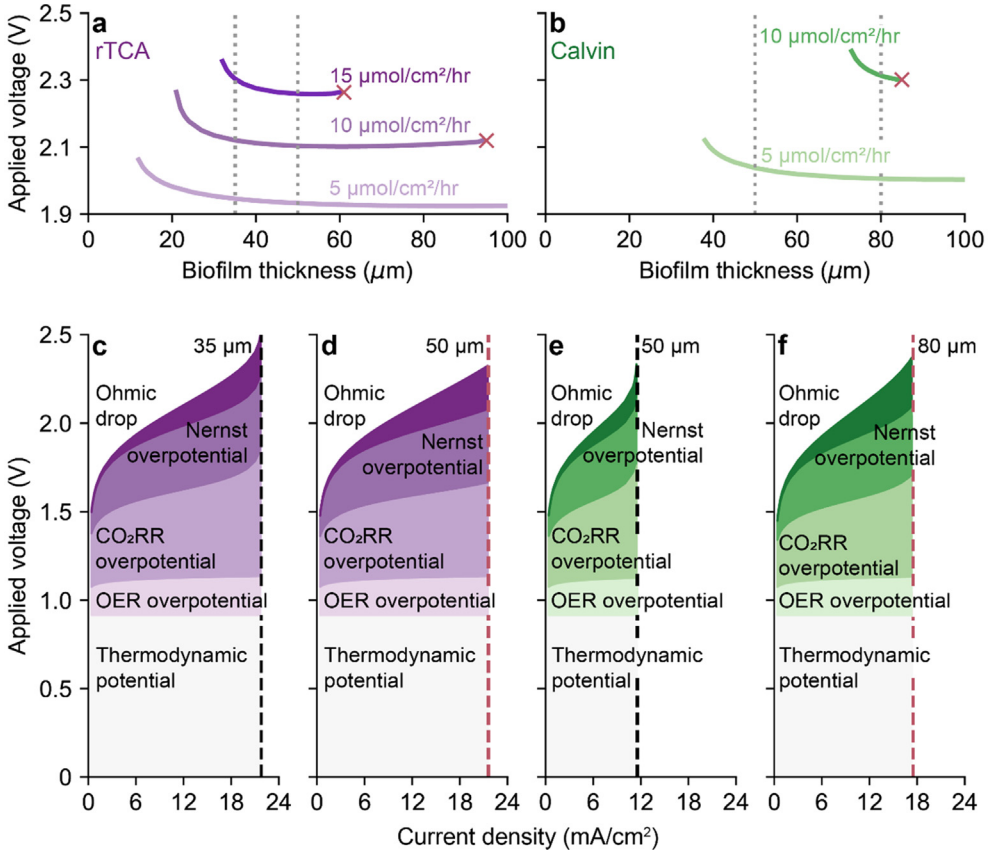


**Fig. 3. Effect of biofilm thickness on reactor operation.** Applied voltage necessary to achieve a specific pyruvate production rate as a function of biofilm thickness for microbes fixing carbon using (**a**) the rTCA cycle and (**b**) the Calvin cycle. Applied voltage breakdown for (**c**) 35 µm, (**d**) 50 µm, (**e**) 50 µm, (**f**) 80 µm biofilms for microbes using the rTCA cycle (**c**, **d**) or Calvin cycle (**e**, **f**). Gray dotted lines in (**a**) and (**b**) correspond to biofilm thicknesses in (**c**–**f**) and were chosen to be representative of different production limits (biomass, $CO_2$ transport). Red crosses in (**a**, **b**) correspond to the $CO_2$ transport limit. Black dashed lines in (**c**, **e**) correspond to biomass-limited current density; red dashed lines in (**d**, **f**) correspond to the $CO_2$ transport-limited current density. Reactor conditions: initial pH = 7.4, 0.25 M $NaNO_3$, D = 5 $hr^{-1}$. (For interpretation of the references to colour in this figure legend, the reader is referred to the web version of this article.)

35-µm film, the difference increases significantly, reaching ~ 200 mV at 21.5 mA/$cm^2$ (~16.9 µmol/$cm^2$/hr) because the activation overpotential for the 35-µm film rises sharply (Fig. 3c). Similar behavior is observed when comparing 50 µm (Fig. 3e) and 80 µm (Fig. 3f) biofilms using the CBB cycle to fix $CO_2$.

### 3.4. Marker gene phylogenetic analysis

Marker gene phylogeny extractions from the Reference Proteomes database resulted in a total of 6918 genomes encoding at least one marker (Fig. 4; Figs. S4-S13; Table S6). Outer membrane cytochromes and their downstream electron transfer components are modular [74,78]. Therefore, although our model focuses on MtrCAB, we extend our genome mining analysis to include other cytochromes capable, or inferred to be capable, of DET, including the whole MtrC/OmcA-family along with the biochemically characterized DmsE/MtrA/PioA/MtoA-, ExtA-, and Cyc2-family proteins (Supplementary note 5). While there is no direct evidence of Cyc2 or MtoA proteins oxidizing a cathode, there is indirect evidence for the oxidation of a cathode by Cyc2 [25,79]. MtoA shares homology with many proteins that have been shown to oxidize a cathode, and these proteins demonstrate reversible electron shuttling (*i.e.*, passage of electrons to or from electrodes). We therefore assume that MtoA is also capable of cathode oxidation and we included both Cyc2 and MtoA in our analysis. We are not aware of a comprehensive multi-heme cytochrome phylogeny that contains all the clades used in this study. Here, we present this phylogeny (Fig. S11), and show the phylogenetic distribution of these cytochromes (Fig. 4). For the cytochrome *c* oxidase phylogenetic tree (Fig. S13), we separated out the low ($aa_3$- and $bo_3$-type) and high ($cbb_3$) affinity cytochrome *c* oxidases into district groups because $cbb_3$ oxidases were found by us and others to be encoded by many microaerophiles that don't grow in $O_2$ concentrations necessary to support reasonable production rates in dEMP [80,81].

We extracted 170 genomes from this dataset that have a complete CBB or rTCA cycle plus at least one electron conduit or that have promise as a chassis for engineering CBB or rTCA-based electrosynthesis (Fig. 5). Of these, 88 organisms have a complete CBB cycle plus at least one electron conduit; genetic engineering methods have been demonstrated in 17 of these organisms. Although 16 organisms have a complete rTCA cycle, only two of these organisms have genetic methods available. The remaining extracted genomes have promise as a chassis for engineering CBB- or rTCA-based electrosynthesis (Fig. 5). In total, 67 genomes encoded both PFOR and OGOR plus at least one electron conduit but were missing AclB/CcsA. Several genomes where completion of the CBB cycle or addition of an electron conduit is feasible were also included.

## 4. Discussion

Our analysis has significant implications for dEMP systems. The model demonstrates that although $O_2$ is a more efficient terminal electron acceptor than $NO_3$–, low $O_2$ solubility limits the productivity of microbes using aerobic respiration. In principle, this issue

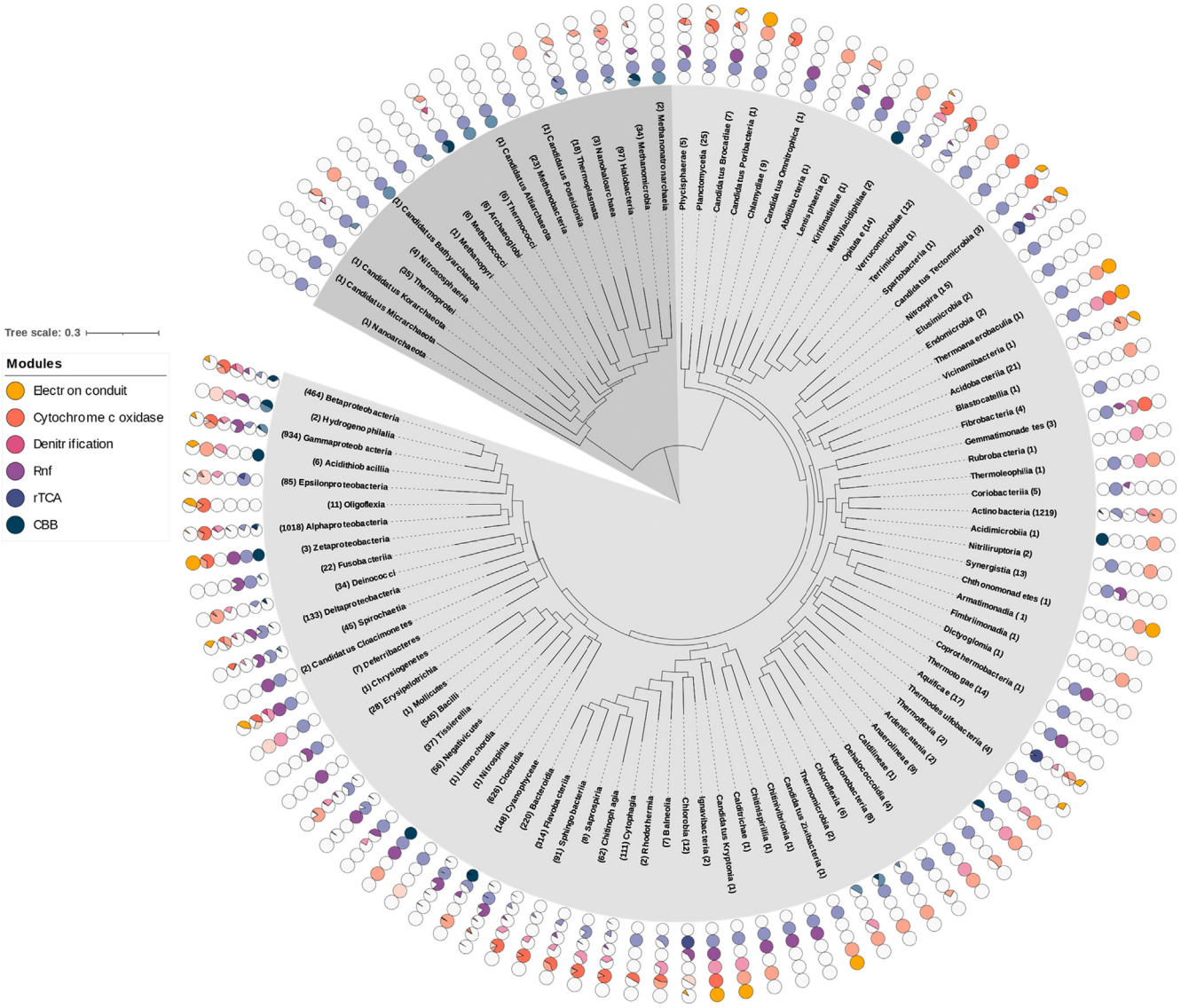


**Fig. 4. Distribution of target metabolic modules in the Reference Proteomes database.** Species were binned by class (or phylum if no class was available), and 16S sequences representing each taxon were used to construct a phylogenetic tree. Each pie chart represents the percentage of species within each taxon that contained the appropriate marker genes. For the CBB (navy), rTCA (indigo), and denitrification (pink) modules, dark colors represent species that had all marker genes, while lighter colors represent species that had at least one, but not the full set of marker genes. The cytochrome *c* oxidase (orange) module shows from lightest to darkest genomes that encode: $cbb_3$ only, $aa_3/bo_3$ only, and both types. The Rnf (purple) module represents the presence of only one marker gene, while the electron conduit (yellow) represents species that had at least one of the four possible marker genes. Archaea are highlighted in dark gray, while bacteria are highlighted in pale gray. (For interpretation of the references to colour in this figure legend, the reader is referred to the web version of this article.)

can be overcome with a carefully designed gas diffusion electrode (GDE). Several criteria must be met simultaneously in this architecture: the GDE would need to be sufficiently hydrophilic to maintain complete wetting with a water film thick enough to support at least a monolayer of cells (>1 μm). However, flooding would displace the vapor phase, so the porosity would have to be high enough to prevent flooding and allow vapor channels for rapid $CO_2$ and $O_2$ diffusion. Future modeling and experimental efforts could identify optimal characteristics for this GDE architecture, which we note would also significantly enhance the $CO_2$-limited productivity described here for standard electrode architectures.

For current designs, $NO_3^-$ respiration is substantially more productive than $O_2$ respiration. In general, soluble terminal electron acceptors such as perchlorate or sulfate should enable higher productivities than $O_2$. However, soluble terminal electron acceptors present two main challenges. First, production of these molecules is typically either energy intensive (in the case of nitrate and perchlorate) or can emit potent greenhouse gases (*e.g.*, nitrous oxide in the case of $NO_3^-$ production). Hence, a comprehensive life cycle analysis of these impacts would be necessary to determine the viability of this production strategy compared to, for example, $H_2$– or formate-mediated electromicrobial production. However, nitrate, perchlorate, and sulfate remediation are all attractive applications of electromicrobial systems independent of commodity chemical production. Second, because $NO_3^-$ (or other soluble terminal electron acceptors) is supplied via the liquid phase, the product titer is restricted by the feed concentration and the stoichiometry of carbon fixation. For example, we assumed an $NO_3^-$ feed concentration of 250 mM. For carbon fixation with the rTCA cycle, this would limit the pyruvate titer to ~33 mM (~3 g/L) because 7.5 $NO_3^-$ molecules are consumed per pyruvate produced (eq. (35) in Methods). This limitation may be partially overcome by enhancing the nitrate tolerance of organisms via adaptive laboratory evolution strategies that have been successful in similar scenarios [82]. We expect

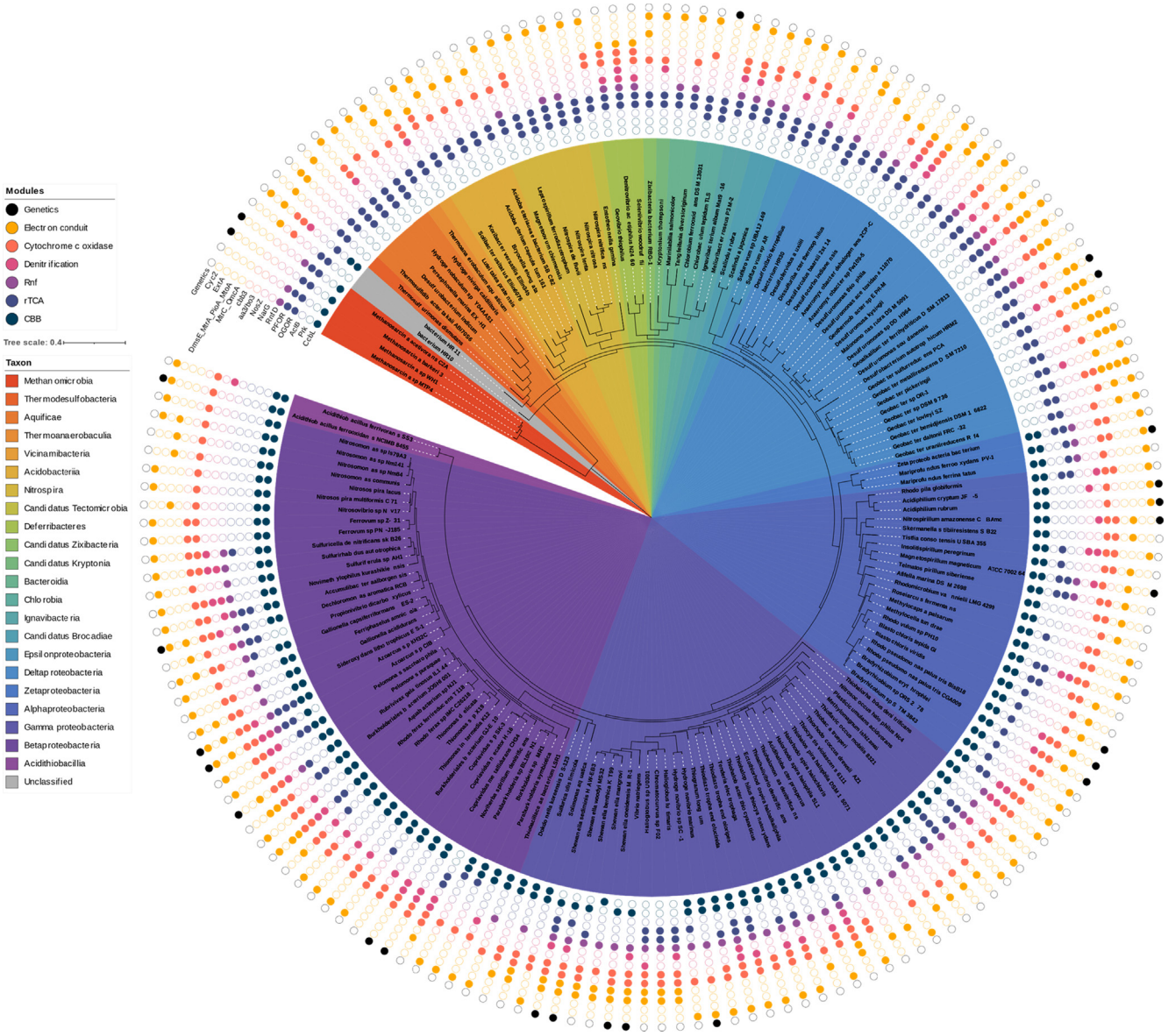


**Fig. 5. Species that are capable of electroautotrophy or that are potential chassis for engineering electroautotrophy.** Marker gene distribution for the CBB (navy) cycle, the rTCA (indigo) cycle, Rnf (purple), denitrification (pink), cytochrome *c* oxidase (orange), and electron conduits (yellow) are displayed on a species-level 16S phylogenetic tree. If a given species has been genetically transformed, that species is marked as having genetic tools (black). (For interpretation of the references to colour in this figure legend, the reader is referred to the web version of this article.)

nitrate to minimize this challenge because it is the most thermodynamically favorable soluble terminal electron acceptor.

Regardless of the terminal electron acceptor, the $CO_2$ transport limit eventually imposes an upper bound on productivity, so increasing biofilm thicknesses cannot enable arbitrarily high production rates. For microbes with a lower enzymatic reaction rate limit (lower turnover number), the steady-state $CO_2$ transport limit is also lower, so microbes using the 3-HP bi-cycle and WLP cannot match the productivity achievable by microbes using the rTCA or CBB cycle regardless of the biofilm thickness. A lower turnover number for the rate-limiting enzyme also increases transport- or activation-associated overpotentials for a given $CO_2$-fixation rate, reducing energy efficiency. Combined, these results indicate that microbes using the rTCA cycle are likely to be both the most productive and most efficient biocatalysts for dEMP systems. Microbes that use the CBB cycle are the second-best option because the biomass-limited reaction rate is much higher even though the cycle's electron utilization efficiency is lower than that for the WLP. Thus, the $CO_2$ transport-limited production rate is higher and transport-associated inefficiencies are lower.

We used a marker protein phylogeny-driven bioinformatics approach to identify organisms capable of electroautotrophy by coupling electron uptake to either $O_2$ or $NO_3^-$ respiration and using either the CBB or rTCA cycles to fix carbon. In our dataset, 72 organisms have complete CBB cycles, NarG and/or $aa_3$/$bo_3$-type cytochrome *c* oxidases, and at least one electron conduit (Fig. 5). Of these, 19 encode NarG (Fig. 5). Our analysis accurately "predicted" four of the six known electroautotrophic bacteria: *A. ferrooxidans* [25], *Rhodopseudomonas palustris* [26], *Candidatus Tenderia electrophaga* [79,83], and *Desulfovibrio ferrophilus* [84] (Fig. 5). One of the bacteria the analysis missed, *Kyrpidia spormannii* [85], was not cultured at the time of our analysis and therefore was not included in the Reference Proteomes Database. The second, *Prosthecochloris aestuarii* [86], was predicted to be autotrophic

(it encodes the rTCA cycle, Table S6), but was not predicted to encode an electron conduit. This indicates that there may be to-date uncharacterized electron conduit proteins, as we discuss later. Interestingly, our analysis also indicated that electroautotrophic capacity could be engineered in *Geobacter sulfurreducens* simply by the introduction of a citrate lyase (aclB/ccsA) gene, a task that was accomplished by Ueki *et al.* with the predicted effect of enabling electroautotrophic growth [87].

Most of the organisms our analysis identifies have not been previously characterized as electroautotrophs. Hence, physiological confirmation of the remaining organisms plus development of genetic tools would significantly expand the available CBB-based electroautotrophs for industrial applications. In contrast, only *Geobacter metallireducens* encodes the rTCA cycle, NarG, and at least one electron conduit. As genetic tools have been developed for *G. metallireducens* [88], this organism represents an especially promising catalyst for industrial dEMP. Because we identified only a small number of organisms that have all the desired modules, most of which do not have genetic tools, we also identified organisms that have potential as synthetic chassis for dEMP, which we discuss here in the context of several possible synthetic biology strategies for engineering electroautotrophy.

First, an organism may have a partial CFP that can be completed by heterologous expression of the missing components. Several recent demonstrations make this an attractive strategy: the CBB cycle has been engineered into heterotrophs by the addition of key enzymes [89–91], and the rTCA cycle was completed in *G. sulfurreducens* to enable electroautotrophy using both rational engineering [87] and directed evolution strategies [92]. An alternate CFP, the reductive glycine pathway [93,94], is a third option since its modularity has recently been confirmed by functional expression in both *Escherichia coli* [95] and *Cupriavidus necator* [96]. Our dataset revealed several organisms in which completion of a partial CFP may be viable. Four of five *Shewanella* species identified in this study encode Prk, three encode partial rTCA cycle markers, and two encode NarG. Given the prevalence of genetic tools available to this genus, the well-characterized use of *Shewanella oneidensis* in bioelectrochemical systems, and facultative anaerobic metabolism, engineering a complete CFP in *Shewanella* could lead to readily-engineerable electroautotrophs. All *Shewanella* species encode the Rnf marker gene, indicating that they can support the efficient reverse-electron transport-driven ferredoxin reduction that may be required for the rTCA cycle.

Second, an organism encoding a complete CFP may be engineered to directly uptake electrons from a cathode. The electron conduit native to *S. oneidensis*, MtrCAB/CymA, has been functionally expressed in *E. coli* [69,97,98], which is a promising host for this strategy since multiple CFPs have been successfully engineered and it naturally respires $NO_3^-$ and $O_2$. Alternatively, *Cupriavidus* spp. encode both a complete CBB cycle, $NO_3^-$ and $O_2$ respiratory modules, and have genetic tools available [99], making these species an attractive option for expressing an electron conduit. Because only two organisms that encode a full rTCA cycle with at least one electron conduit have genetic methods available, the green sulfur bacterium *Chlorobaculum tepidum*, which encodes the full rTCA and has genetic tools, may be another suitable host for electron conduit expression.

Finally, an organism with a complete CFP and a functional electron conduit may be engineered to use an alternate electron acceptor. We use $NO_3^-$ respiration in our model since it is the most thermodynamically favorable soluble electron acceptor; $NO_3^-$ respiration could be introduced into organisms by expressing the NarGHI complex. However, 5 molybdopterin cofactor biosynthesis enzymes are also necessary for proper functioning of this complex, so an appropriate chassis would benefit significantly from natural expression of these supporting proteins. *R. palustris* is an excellent candidate for this strategy since it has a well-characterized electron conduit [26], a complete CBB cycle, and encodes the molybdopterin biosynthesis genes. This organism has been engineered for *poly*-hydroxybutyrate [100] and *n*-butanol [101] production in dEMP systems, so heterologous expression of NarGHI may enable higher yields and productivities. *Azoarcus* sp. KH32C has complete CBB and rTCA cycles and encodes NosZ, while lacking NarG. A genetic system was developed in the related *Azoarcus* sp. strain BH72 [102], which may open up KH32C for heterologous expression of NarGHI, further increasing the potential of this species for dEMP.

The multiheme cytochrome phylogeny developed here (Fig. S11) indicates that a significant number of undiscovered cytochromes that support electron exchange with an electrode may exist. This hypothesis is supported by reports of direct electron uptake independent of the four biochemically characterized families of outer membrane cytochromes used in our study; for example, both the methanogenic archaeon *Methanosarcina barkeri* [103] and the green sulfur bacterium *P. aestuarii* [86] have been shown to directly accept electrons from a cathode. Cytochromes involved in direct electron transfer may therefore be more widespread and diverse than currently realized, opening the possibility of a significant number of additional chassis for dEMP.

## 5. Outlook

Here we have identified several microbial chassis that have potential as industrial dEMP strains (Table 1) and outlined a series of Technology Readiness Levels (TRLs) to evaluate industrial relevance of microbial catalysts (Table S7). Beyond the genetic modules that enable electroautotrophy, additional factors constrain the productivity achievable by a given organism. For current densities > 10 mA/cm$^2$, which are likely necessary for viable production capacity, our model predicts alkaline conditions throughout the biofilm, indicating that (facultative) alkalophilicity is a desirable trait in the ideal strain. A higher salinity reduces Ohmic overpotential and an increased bicarbonate concentration can enhance productivity by aiding $CO_2$ transport, so halophilicity or halotolerance is similarly advantageous. Unfortunately, the pH- and halo-tolerance of the organisms we identify is unclear, so future studies, in addition to confirming electroautotrophic capacity, should also characterize these traits. A suitable microbial catalyst could also be engineered to tolerate alkaline or saline conditions using rational engineering or directed evolution strategies [82,104]. Temperature effects may also play an important role in improving the productivity of dEMP systems, as has been suggested previously [105]. Several competing effects on the kinetics and thermodynamics of electron transfer, $CO_2$ solubility and diffusivity, and acid-base equilibria make this an interesting direction for future modeling efforts following the framework developed here and can be tailored to conditions suitable for known or predicted thermophilic electroautotrophs such as *K. spormannii* [85], *Thermoanaerobaculum aquaticum* (Fig. 5) or *Chlorobaculum tepidum* (Fig. 5). Because the turnover number of the rate-limiting enzyme plays a key role in setting productivity and efficiency limits for dEMP, these values should also be characterized in the organism (s) of interest. Strain engineering can then focus on increasing the rate limit either by increasing the enzyme turnover number or overexpressing the rate-limiting enzyme.

Strain selection and engineering should also be guided by the desired product. For example, the CBB cycle is well-suited for the production of sugars such as sucrose because its end product is glyceraldehyde-3-phosphate, while the rTCA cycle may be better suited to fatty acid production since the end product, acetyl-CoA, is used directly by fatty acid biosynthesis pathways. Future work

**Table 1**
Promising microbial chassis for dEMP.

| Organism | TRL[†] | Complete CFP | Engineered CFP |
|---|---|---|---|
| *Geobacter metallireducens* | 1 | rTCA | – |
| *Geobacter sulfurreducens* | 3 | – | *rTCA [87,92] |
| *Escherichia coli* | 1 | – | *CBB [89] and *rGly [95] |
| *Cupriavidus necator* | 1 | CBB | *rGly [96] |
| *Shewanella oneidensis* | 1 | – | rTCA or CBB |
| *Shewanella sediminis* | 1 | – | rTCA or CBB |
| *Shewanella woodii* | 1 | – | rTCA or CBB |
| *Vibrio natriegens* | 1 | – | CBB |
| *Chlorobaculum tepidum* | 1 | rTCA | – |
| *Rhodopseudomonas palustris* | 4 | CBB | – |
| *Azoarcus* sp. KH32C | 1 | rTCA and CBB | – |
| *Methanosarcina barkeri* | 1 | WL | rTCA or CBB |
| *Methanosarcina acetivorans* | 1 | WL | rTCA or CBB |

[†] Scale: 1, least ready; 5 most ready (Table S7).
* Denotes experimental demonstration of engineered CFP.

to determine optimal chassis for a given product can apply elementary mode analysis or other metabolic engineering approaches following previous efforts by Kracke et al. [106,107].

## Author Contributions

Anthony J. Abel and Jacob M. Hilzinger developed the physiology, analyzed the data, and wrote the manuscript. Anthony J. Abel built the model. Jacob M. Hilzinger performed the phylogenetic analysis. Adam P. Arkin and Douglas S. Clark edited the manuscript and supervised the project.

## Declaration of Competing Interest

The authors declare that they have no known competing financial interests or personal relationships that could have appeared to influence the work reported in this paper.

## Acknowledgements

This work was supported by the Center for the Utilization of Biological Engineering in Space (CUBES, https://cubes.space), a NASA Space Technology Research Institute (grant number NNX17AJ31G). A.J.A. is supported by an NSF Graduate Research Fellowship under grant number DGE 1752814. We thank Dr. Lien-Chun Weng (UC Berkeley) for advice on COMSOL modeling, Helen Bergstrom (UC Berkeley) for useful discussions on electrochemistry, and Dr. Paul Tol (Netherlands Institute for Space Research, SRON) for a helpful reference on accessible color schemes (-https://personal.sron.nl/~pault/).

## Appendix A. Supplementary data

Data and code used to generate figures and COMSOL models are available at https://doi.org/10.6084/m9.figshare.

## References

[1] R.E. Blankenship et al., Comparing photosynthetic and photovoltaic efficiencies and recognizing the potential for improvement, Science 332 (2011) 805–809.
[2] J.M. Spurgeon, B. Kumar, A comparative technoeconomic analysis of pathways for commercial electrochemical $CO_2$ reduction to liquid products, Energy Environ. Sci. 11 (2018) 1536–1551.
[3] W. Sheng et al., Electrochemical reduction of $CO_2$ to synthesis gas with controlled CO/$H_2$ ratios, Energy Environ. Sci. 10 (2017) 1180–1185.
[4] P. De Luna, C. Hahn, D. Higgins, S.A. Jaffer, T.F. Jaramillo, E.H. Sargent, What would it take for renewably powered electrosynthesis to displace petrochemical processes?, Science 364 (6438) (2019), https://doiorg/10.1126/science:aav3506.
[5] Z. Liu, K. Wang, Y. Chen, T. Tan, J. Nielsen, Third-generation biorefineries as the means to produce fuels and chemicals from $CO_2$, Nat. Catal. 3 (2020) 274–288.
[6] N.J. Claassens, D.Z. Sousa, V.A.P.M. Dos Santos, W.M. De Vos, J. Van Der Oost, Harnessing the power of microbial autotrophy, Nat. Rev. Microbiol. 14 (2016) 692–706.
[7] N.J. Claassens, C.A.R. Cotton, D. Kopljar, A. Bar-Even, Making quantitative sense of electromicrobial production, Nat. Catal. 2 (2019) 437–447.
[8] U. Schröder, F. Harnisch, L.T. Angenent, Microbial electrochemistry and technology: terminology and classification, Energy Environ. Sci. 8 (2015) 513–519.
[9] C. Liu, B.C. Colón, M. Ziesack, P.A. Silver, D.G. Nocera, Water splitting–biosynthetic system with $CO_2$ reduction efficiencies exceeding photosynthesis, Science 352 (2016) 1210–1213.
[10] H. Li et al., Integrated electromicrobial conversion of $CO_2$ to higher alcohols, Science 335 (2012) 1596.
[11] N.J. Claassens, I. Sánchez-Andrea, D.Z. Sousa, A. Bar-Even, Towards sustainable feedstocks: a guide to electron donors for microbial carbon fixation, Curr. Opin. Biotechnol. 50 (2018) 195–205.
[12] L.C. Weng, A.T. Bell, A.Z. Weber, Towards membrane-electrode assembly systems for CO2 reduction: a modeling study, Energy Environ. Sci. 12 (2019) 1950–1968.
[13] L.C. Weng, A.T. Bell, A.Z. Weber, Modeling gas-diffusion electrodes for $CO_2$ reduction, Phys. Chem. Chem. Phys. 20 (2018) 16973–16984.
[14] K. Tran, Z.W. Ulissi, Active learning across intermetallics to guide discovery of electrocatalysts for $CO_2$ reduction and H2 evolution, Nat. Catal. 1 (2018) 696–703.
[15] A.J. Abel, D.S. Clark, A comprehensive modeling analysis of formate-mediated microbial electrosynthesis, ChemSusChem 14 (1) (2021) 344–355.
[16] Y. Chen et al., A robust, scalable platform for the electrochemical conversion of $CO_2$ to formate: identifying pathways to higher energy efficiencies, ACS Energy Lett. 5 (2020) 1825–1833.
[17] R. Hegner, K. Neubert, C. Kroner, D. Holtmann, F. Harnisch, Coupled electrochemical and microbial catalysis for the production of polymer bricks, ChemSusChem 13 (19) (2020) 5295–5300.
[18] A. Tanaka, M. Hirata, Y. Kiyohara, M. Nakano, K. Omae, M. Shiratani, K. Koga, Review of pulmonary toxicity of indium compounds to animals and humans, Thin Solid Films 518 (11) (2010) 2934–2936.
[19] R.G. Grim et al., Transforming the carbon economy: challenges and opportunities in the convergence of low-cost electricity and reductive $CO_2$ utilization, Energy Environ. Sci. 13 (2020) 472–494.
[20] A.A. Menezes, J. Cumbers, J.A. Hogan, A.P. Arkin, Towards synthetic biological approaches to resource utilization on space missions, J. R. Soc. Interface 12 (102) (2015) 20140715, https://doi.org/10.1098/rsif.2014.0715.
[21] L. Jourdin, J. Sousa, N.V. Stralen, D.P.B.T.B. Strik, Techno-economic assessment of microbial electrosynthesis from $CO_2$ and/or organics: an interdisciplinary roadmap towards future research and application, Appl. Energy 279 (2020) 115775, https://doi.org/10.1016/j.apenergy.2020.115775.
[22] A. Prévoteau, J.M. Carvajal-Arroyo, R. Ganigué, K. Rabaey, Microbial electrosynthesis from $CO_2$: forever a promise?, Curr Opin. Biotechnol. 62 (2020) 48–57.
[23] D.D. Nayak, W.W. Metcalf, Cas9-mediated genome editing in the methanogenic archaeon Methanosarcina acetivorans, Proc. Natl. Acad. Sci. USA 114 (2017) 2976–2981.
[24] C. Leang, T. Ueki, K.P. Nevin, D.R. Lovley, A Genetic system for Clostridium ljungdahlii: A chassis for autotrophic production of biocommodities and a model homoacetogen, Appl. Environ. Microbiol. 79 (2013) 1102–1109.
[25] T. Ishii, S. Kawaichi, H. Nakagawa, K. Hashimoto, R. Nakamura, From chemolithoautotrophs to electrolithoautotrophs: $CO_2$ fixation by Fe(II)-oxidizing bacteria coupled with direct uptake of electrons from solid electron sources, Front. Microbiol. 6 (2015) 994.
[26] D. Gupta, M.C. Sutherland, K. Rengasamy, J.M. Meacham, R.G. Kranz, A. Bose, A. Komeili, Photoferrotrophs produce a PioAB electron conduit for extracellular electron uptake, MBio 10 (6) (2019), https://doi.org/10.1128/mBio.02668-19.
[27] M.D. Yates, L.J. Bird, B.J. Eddie, E.L. Onderko, C.A. Voigt, S.M. Glaven, Nanoliter scale electrochemistry of natural and engineered electroactive bacteria, Bioelectrochemistry 137 (2021) 107644, https://doi.org/10.1016/j.bioelechem.2020.107644.
[28] M. Tahernia et al., A 96-well high-throughput, rapid-screening platform of extracellular electron transfer in microbial fuel cells, Biosens. Bioelectron. 162 (2020) 112259.
[29] B. Korth, L.F.M. Rosa, F. Harnisch, C. Picioreanu, A framework for modeling electroactive microbial biofilms performing direct electron transfer, Bioelectrochemistry 106 (2015) 194–206.
[30] A.C.L. De Lichtervelde, A. Ter Heijne, H.V.M. Hamelers, P.M. Biesheuvel, J.E. Dykstra, Theory of ion and electron transport coupled with biochemical conversions in an electroactive biofilm, Phys. Rev. Appl. 12 (2019) 14018.
[31] F. Salimijazi, J. Kim, A.M. Schmitz, R. Grenville, A. Bocarsly, B. Barstow, Constraints on the efficiency of engineered electromicrobial production, Joule 4 (10) (2020) 2101–2130.
[32] A.R. Rowe, P. Rajeev, A. Jain, S. Pirbadian, A. Okamoto, J.A. Gralnick, M.Y. El-Naggar, K.H. Nealson, M.W. Ribbe, C. Ajo-Franklin, B. Barstow, Tracking electron uptake from a cathode into Shewanella cells: implications for energy

acquisition from solid-substrate electron donors, MBio 9 (1) (2018), https://doi.org/10.1128/mBio.02203-17.
[33] A.G. Fast, E.T. Papoutsakis, Stoichiometric and energetic analyses of non-photosynthetic $CO_2$-fixation pathways to support synthetic biology strategies for production of fuels and chemicals, Curr. Opin. Chem. Eng. 1 (2012) 380–395.
[34] J.S. Newman, C.W. Tobias, Theoretical analysis of current distribution in porous electrodes, J. Electrochem. Soc. 109 (1962) 1183.
[35] Z. Yang et al., Modeling and upscaling analysis of gas diffusion electrode-based electrochemical carbon dioxide reduction systems, ACS Sustain. Chem. Eng. 9 (2021) 351–361.
[36] M.R. Singh, E.L. Clark, A.T. Bell, Effects of electrolyte, catalyst, and membrane composition and operating conditions on the performance of solar-driven electrochemical reduction of carbon dioxide, Phys. Chem. Chem. Phys. 17 (2015) 18924–18936.
[37] U. Riebesell, V.J. Fabry, L. Hansson, J.-P. Gattuso, Guide to best practices for ocean acidification research and data reporting, Publications Office of the European Union Luxembourg (2011), https://doi.org/10.2777/66906.
[38] S. Haussener et al., Modeling, simulation, and design criteria for photoelectrochemical water-splitting systems, Energy Environ. Sci. 5 (2012) 9922–9935.
[39] P.M. Wilt, Nucleation rates and bubble stability in water-carbon dioxide solutions, J. Colloid Interface Sci. 112 (2) (1986) 530–538.
[40] M. Lin, L. Han, M.R. Singh, C. Xiang, An experimental- and simulation-based evaluation of the $CO_2$ utilization efficiency of aqueous-based electrochemical $CO_2$ reduction reactors with ion-selective membranes, ACS Appl. Energy Mater. 2 (2019) 5843–5850.
[41] A.R. Rowe et al., Identification of a pathway for electron uptake in Shewanella oneidensis, Commun. Biol. 4 (2021) 957.
[42] D.E. Ross, J.M. Flynn, D.B. Baron, J.A. Gralnick, D.R. Bond, S.-Y. Xu, Towards electrosynthesis in Shewanella: Energetics of reversing the Mtr pathway for reductive metabolism, PLoS ONE 6 (2) (2011) e16649.
[43] M.N. Alves et al., Characterization of the periplasmic redox network that sustains the versatile anaerobic metabolism of Shewanella oneidensis MR-1, Front. Microbiol. 6 (2015) 665.
[44] F. Kracke, I. Vassilev, J.O. Krömer, Microbial electron transport and energy conservation - The foundation for optimizing bioelectrochemical systems, Front. Microbiol. 6 (2015) 1–18.
[45] P. Mitchell, Possible molecular mechanisms of the protonmotive function of cytochrome systems, J. Theor. Biol. 62 (2) (1976) 327–367.
[46] C. Lange, C. Hunte, Crystal structure of the yeast cytochrome bc1 complex with its bound substrate cytochrome c, Proc. Natl. Acad. Sci. USA 99 (2002) 2800–2805.
[47] M. Saraste, Oxidative phosphorylation at the fin de siecle, Science 283 (1999) 1488–1493.
[48] C. Moreno-Vivián, Purificación Cabello, M. Martínez-Luque, R. Blasco, F. Castillo, Prokaryotic nitrate reduction: Molecular properties and functional distinction among bacterial nitrate reductases, J. Bacteriol. 181 (21) (1999) 6573–6584.
[49] I.A. Berg, Ecological aspects of the distribution of different autotrophic $CO_2$ fixation pathways, Appl. Environ. Microbiol. 77 (6) (2011) 1925–1936.
[50] T. Yagi, The bacterial energy-transducing NADH-quinone oxidoreductases, Biochim. Biophys. Acta - Bioenerg. 1141 (1) (1993) 1–17.
[51] PETER Mitchell, Chemiosmotic coupling in oxidative and photosynthetic phosphorylation, Biol. Rev. Camb. Philos. Soc. 41 (3) (1966) 445–501.
[52] E. Biegel, S. Schmidt, J.M. González, V. Müller, Biochemistry, evolution and physiological function of the Rnf complex, a novel ion-motive electron transport complex in prokaryotes, Cell. Mol. Life Sci. 68 (2011) 613–634.
[53] P.-L. Tremblay, T. Zhang, S.A. Dar, C. Leang, D.R. Lovley, D.K. Newman, The Rnf complex of Clostridium ljungdahlii is a proton-translocating ferredoxin: NAD + oxidoreductase essential for autotrophic growth, MBio 4 (1) (2013), https://doi.org/10.1128/mBio.00406-12.
[54] M. Rubin-Blum, N. Dubilier, M. Kleiner, S.J. Hallam, Genetic Evidence for Two Carbon Fixation Pathways (the Calvin-Benson-Bassham Cycle and the Reverse Tricarboxylic Acid Cycle) in Symbiotic and Free-Living Bacteria, mSphere 4 (1) (2019), https://doi.org/10.1128/mSphere.00394-18.
[55] J. Newman, K.E. Thomas-Alyea, Electrochemical Systems, Wiley, 2004.
[56] B.J. Campbell, S.C. Gary, Abundance of reverse tricarboxylic acid cycle genes in free-living microorganisms at deep-sea hydrothermal vents, Appl. Environ. Microbiol. 70 (2004) 6282–6289.
[57] E. Kandeler, K. Deiglmayr, D. Tscherko, D. Bru, L. Philippot, Abundance of narG, nirS, nirK, and nosZ genes of denitrifying bacteria during primary successions of a glacier foreland, Appl. Environ. Microbiol. 72 (2006) 5957–5962.
[58] M. Hügler, S.M. Sievert, Beyond the Calvin cycle: Autotrophic carbon fixation in the ocean, Ann. Rev. Mar. Sci. 3 (2011) 261–289.
[59] L.S. Johnson, S.R. Eddy, E. Portugaly, Hidden Markov model speed heuristic and iterative HMM search procedure, BMC Bioinf. 11 (1) (2010), https://doi.org/10.1186/1471-2105-11-431.
[60] K. Katoh, D.M. Standley, MAFFT multiple sequence alignment software version 7: Improvements in performance and usability, Mol. Biol. Evol. 30 (2013) 772–780.
[61] K. Katoh, J. Rozewicki, K.D. Yamada, MAFFT online service: Multiple sequence alignment, interactive sequence choice and visualization, Brief. Bioinform. 20 (2018) 1160–1166.
[62] M.N. Price, P.S. Dehal, A.P. Arkin, A.F.Y. Poon, FastTree 2 - Approximately maximum-likelihood trees for large alignments, PLoS ONE 5 (3) (2010) e9490.
[63] R.M. Moore, A.O. Harrison, S.M. McAllister, S.W. Polson, K.E. Wommack, Iroki: automatic customization and visualization of phylogenetic trees, PeerJ 8 (2020) e8584.
[64] M.I. Gibson, P.Y.T. Chen, C.L. Drennan, A structural phylogeny for understanding 2-oxoacid oxidoreductase function, Curr. Opin. Struct. Biol. 41 (2016) 54–61.
[65] Price, M. N. & Arkin, A. P. PaperBLAST: Text Mining Papers for Information about Homologs. *mSystems* **2**, 1–10 (2017).
[66] E. Paradis, K. Schliep, R. Schwartz, Ape 5.0: An environment for modern phylogenetics and evolutionary analyses in R, Bioinformatics 35 (3) (2019) 526–528.
[67] I. Letunic, P. Bork, Interactive Tree of Life (iTOL) v4: Recent updates and new developments, Nucleic Acids Res. 47 (2019) 256–259.
[68] Coursolle, D., Baron, D.B., Bond, D.R., Gralnick, J.A. (2010). The Mtr respiratory pathway is essential for reducing flavins and electrodes in Shewanella oneidensis. J. Bacteriol. 192, 467–474 (2010).
[69] D. Coursolle, J.A. Gralnick, Modularity of the mtr respiratory pathway of shewanella oneidensis strain MR-1, Mol. Microbiol. 77 (2010) 995–1008.
[70] Y. Jiao, D.K. Newman, The pio operon is essential for phototrophic Fe(II) oxidation in Rhodopseudomonas palustris TIE-1, J. Bacteriol. 189 (2007) 1765–1773.
[71] J. Liu et al., Identification and characterization of MtoA: A decaheme c-type cytochrome of the neutrophilic Fe(ll)-oxidizing bacterium Sideroxydans lithotrophicus ES-1, Front. Microbiol. 3 (2012) 1–11.
[72] J.A. Gralnick, H. Vali, D.P. Lies, D.K. Newman, Extracellular respiration of dimethyl sulfoxide by Shewanella oneidensis strain MR-1, Proc. Natl. Acad. Sci. USA 103 (2006) 4669–4674.
[73] F. Jiménez Otero, C.H. Chan, D.R. Bond, Identification of Different Putative Outer Membrane Electron Conduits Necessary for Fe(III) Citrate, Fe(III) Oxide, Mn(IV) Oxide, or Electrode Reduction by Geobacter sulfurreducens, J. Bacteriol. 200 (2018) 1–20.
[74] D. Gupta, M.S. Guzman, A. Bose, Extracellular electron uptake by autotrophic microbes: physiological, ecological, and evolutionary implications, J. Ind. Microbiol. Biotechnol. 47 (2020) 863–876.
[75] T. Zhang et al., Improved cathode materials for microbial electrosynthesis, Energy Environ. Sci. 6 (2013) 217–224.
[76] M. Cui, H. Nie, T. Zhang, D. Lovley, T.P. Russell, Three-dimensional hierarchical metal oxide-carbon electrode materials for highly efficient microbial electrosynthesis, Sustain. Energy Fuels 1 (2017) 1171–1176.
[77] L. Jourdin et al., High acetic acid production rate obtained by microbial electrosynthesis from carbon dioxide, Environ. Sci. Technol. 49 (2015) 13566–13574.
[78] B.E. Conley, M.T. Weinstock, D.R. Bond, J.A. Gralnick, R.M. Kelly, A hybrid extracellular electron transfer pathway enhances the survival of vibrio natriegens, Appl. Environ. Microbiol. 86 (19) (2020), https://doi.org/10.1128/AEM.01253-20.
[79] B.J. Eddie, Z. Wang, W.J. Hervey, D.H. Leary, A.P. Malanoski, L.M. Tender, B. Lin, S.M. Strycharz-Glaven, K. Rabaey, Metatranscriptomics Supports the Mechanism for Biocathode Electroautotrophy by " Candidatus Tenderia electrophaga", mSystems 2 (2) (2017), https://doi.org/10.1128/mSystems.00002-17.
[80] M.M. Pereira, M. Santana, M. Teixeira, A novel scenario for the evolution of haem–copper oxygen reductases, Biochim. Biophys. Acta - Bioenerg. 1505 (2-3) (2001) 185–208.
[81] R.S. Pitcher, N.J. Watmough, The bacterial cytochrome cbb3 oxidases, Biochim. Biophys. Acta - Bioenerg. 1655 (2004) 388–399.
[82] X. Wu, R. Altman, M.A. Eiteman, E. Altman, Adaptation of escherichia coli to elevated sodium concentrations increases cation tolerance and enables greater lactic acid production, Appl. Environ. Microbiol. 80 (2014) 2880–2888.
[83] A.P. Malanoski et al., Relative abundance of 'Candidatus Tenderia electrophaga' is linked to cathodic current in an aerobic biocathode community, Microb. Biotechnol. 11 (2018) 98–111.
[84] X. Deng, N. Dohmae, K.H. Nealson, K. Hashimoto, A. Okamoto, Multi-heme cytochromes provide a pathway for survival in energy-limited environments, Sci. Adv. 4 (2) (2018), https://doi.org/10.1126/sciadv.aao5682.
[85] J.E. Reiner et al., From an extremophilic community to an electroautotrophic production strain: identifying a novel Knallgas bacterium as cathodic biofilm biocatalyst, ISME J. 14 (2020) 1125–1140.
[86] P.T. Ha et al., Syntrophic anaerobic photosynthesis via direct interspecies electron transfer, Nat. Commun. 8 (2017) 1–7.
[87] T. Ueki et al., Construction of a geobacter strain with exceptional growth on cathodes, Front. Microbiol. 9 (2018) 1512.
[88] P.L. Tremblay, M. Aklujkar, C. Leang, K.P. Nevin, D. Lovley, A genetic system for Geobacter metallireducens: Role of the flagellin and pilin in the reduction of Fe(III) oxide, Environ. Microbiol. Rep. 4 (2012) 82–88.
[89] S. Gleizer, R. Ben-Nissan, Y.M. Bar-On, N. Antonovsky, E. Noor, Y. Zohar, G. Jona, E. Krieger, M. Shamshoum, A. Bar-Even, R. Milo, Conversion of Escherichia coli to Generate All Biomass Carbon from $CO_2$, Cell 179 (6) (2019) 1255–1263.e12.
[90] A.I. Flamholz, E. Dugan, C. Blikstad, S. Gleizer, R. Ben-Nissan, S. Amram, N. Antonovsky, S. Ravishankar, E. Noor, A. Bar-Even, R. Milo, D.F. Savage,

Functional reconstitution of a bacterial $CO_2$ concentrating mechanism in Escherichia coli, Elife 9 (2020), https://doi.org/10.7554/eLife.59882.
[91] T. Gassler et al., The industrial yeast Pichia pastoris is converted from a heterotroph into an autotroph capable of growth on $CO_2$, Nat. Biotechnol. 38 (2020) 210–216.
[92] T. Zhang, X.C. Shi, R. Ding, K. Xu, P.L. Tremblay, The hidden chemolithoautotrophic metabolism of Geobacter sulfurreducens uncovered by adaptation to formate, ISME J. 14 (2020) 2078–2089.
[93] A. Bar-Even, E. Noor, A. Flamholz, R. Milo, Design and analysis of metabolic pathways supporting formatotrophic growth for electricity-dependent cultivation of microbes, Biochim. Biophys. Acta - Bioenerg. 1827 (2013) 1039–1047.
[94] I. Sánchez-Andrea, I.A. Guedes, B. Hornung, S. Boeren, C.E. Lawson, D. Z. Sousa, A. Bar-Even, N.J. Claassens, A.J.M. Stams, The reductive glycine pathway allows autotrophic growth of Desulfovibrio desulfuricans, Nat. Commun. 11 (1) (2020), https://doi.org/10.1038/s41467-020-18906-7.
[95] S. Kim et al., Growth of E. coli on formate and methanol via the reductive glycine pathway, Nat. Chem. Biol. 16 (2020) 538–545.
[96] N.J. Claassens et al., Replacing the Calvin cycle with the reductive glycine pathway in Cupriavidus necator, Metab. Eng. 62 (2020) 30–41.
[97] H.M. Jensen, A.E. Albers, K.R. Malley, Y.Y. Londer, B.E. Cohen, B.A. Helms, P. Weigele, J.T. Groves, C.M. Ajo-Franklin, Engineering of a synthetic electron conduit in living cells, Proc. Natl. Acad. Sci. 107 (45) (2010) 19213–19218.
[98] H.M. Jensen, M.A. TerAvest, M.G. Kokish, C.M. Ajo-Franklin, CymA and exogenous flavins improve extracellular electron transfer and couple it to cell Growth in Mtr-expressing Escherichia coli, ACS Synth. Biol. 5 (2016) 679–688.
[99] C. Bi et al., Development of a broad-host synthetic biology toolbox for ralstonia eutropha and its application to engineering hydrocarbon biofuel production, Microb. Cell Fact. 12 (2013) 1–10.
[100] T.O. Ranaivoarisoa, R. Singh, K. Rengasamy, M.S. Guzman, A. Bose, Towards sustainable bioplastic production using the photoautotrophic bacterium Rhodopseudomonas palustris TIE-1, J. Ind. Microbiol. Biotechnol. 46 (2019) 1401–1417.
[101] Bai, W., Ranaivoarisoa, T. O., Singh, R., Rengasamy, K. & Bose, A. Sustainable Production of the Biofuel n-Butanol by Rhodopseudomonas palustris TIE-1. *bioRxiv* (2020). doi:10.1101/2020.10.13.336636.
[102] M. Böhm, T. Hurek, B. Reinhold-Hurek, Twitching motility is essential for endophytic rice colonization by the $N_2$-fixing endophyte Azoarcus sp. strain BH72, Mol. Plant-Microbe Interact. 20 (2007) 526–533.
[103] A.R. Rowe, S. Xu, E. Gardel, A. Bose, P. Girguis, J.P. Amend, M.Y. El-Naggar, M. W. Ribbe, Methane-linked mechanisms of electron uptake from cathodes by Methanosarcina barkeri, MBio 10 (2) (2019), https://doi.org/10.1128/mBio.02448-18.
[104] I. Hamdallah, N. Torok, K.M. Bischof, N. Majdalani, S. Chadalavada, N. Mdluli, K.E. Creamer, M. Clark, C. Holdener, P.J. Basting, S. Gottesman, J.L. Slonczewski, R.E. Parales, Experimental evolution of Escherichia coli K-12 at high pH and with RpoS induction, Appl. Environ. Microbiol. 84 (15) (2018), https://doi.org/10.1128/AEM.00520-18.
[105] L. Jourdin, T. Burdyny, Microbial electrosynthesis: where do we go from here?, Trends Biotechnol 1–11 (2020).
[106] F. Kracke, B. Lai, S. Yu, J.O. Krömer, Balancing cellular redox metabolism in microbial electrosynthesis and electro fermentation – a chance for metabolic engineering, Metab. Eng. 45 (2018) 109–120.
[107] F. Kracke, J.O. Krömer, Identifying target processes for microbial electrosynthesis by elementary mode analysis, BMC Bioinf. 15 (2014) 1–14.